How to perform admittance spectroscopy and DLTS in multijunction solar cells

Cyril Leon [a,b,c,*], Sylvain Le Gall [a,b,c], Marie-Estelle Gueunier-Farret [a,b,c], Jean-Paul Kleider [a,b,c]

[a] *Université Paris-Saclay, CentraleSupélec, CNRS, Laboratoire de Génie Electrique et Electronique de Paris, 91192, Gif-sur-Yvette, France*
[b] *Sorbonne Université, CNRS, Laboratoire de Génie Electrique et Electronique de Paris, 75252, Paris, France*
[c] *IPVF, Institut Photovoltaïque D'Ile-de-France, 91120, Palaiseau, France*

A B S T R A C T

We propose a simple and non-destructive method to access the properties of the defects within the subcells of multijunction solar cells (MJSC) based on the extension of two well-known techniques, namely Admittance Spectroscopy (AS) and Deep-Level Transient Spectroscopy (DLTS). Due to the electrical coupling between the subcells of an MJSC, the AS and DLTS signatures of the defects present in the subcells are difficult to identify and to properly analyse, and other independent phenomena could be misinterpreted as such. From numerical simulations and theoretical developments, it is shown how the use of dedicated experimental conditions, in particular specific light biases, on MJSCs can reveal the signatures of the defects present in each subcell and allow one to analyse them without misinterpretation.

1. Introduction

Multijunction solar cells (MJSCs) offer the possibility to overcome the Shockley-Queisser limit for a single junction solar cell and can reach efficiencies above 30% [1]. Among the best MJSCs, performance records are achieved when several III-V materials subcells are combined: 39.2% for a six junction-solar cell, 38.8% for a five-junction solar cell, 37.9% for a triple-junction solar cell and 32.8% for a tandem solar cell (TSC) under 1-sun illumination [2–5]. Regarding the triple junctions and the tandem solar cells, technologies combining III-V and Si materials also offer interesting efficiencies: 35.9% et 32.8% for cells associating three subcells (GaInP/GaAs/Si) and two subcells (GaAs/Si), respectively [6]. In most cases, in a MJSC the subcells are monolithically stacked and electrically coupled. This coupling results in difficulties to characterize the MJSC at the subcell level which is important to optimize the fabrication processes or understand the mechanism causing the degradation of the solar cells [7].

Admittance Spectroscopy (AS) and Deep-Level Transient Spectroscopy (DLTS) are two well-known characterisation techniques that provide information on the defects causing intermediate states in the bandgap energy of the materials [8–10]. Admittance spectroscopy refers to the measurement as a function of frequency and temperature of the current in a device submitted to a small alternative bias change, from which one can derive the equivalent parallel junction capacitance, C, and parallel conductance G. DLTS uses the transient response of the device following a voltage pulse and exploits the temperature dependence of the transient of the current or of the junction capacitance. They have been widely used for solar cells applications [11–31]. However, in MJSCs, the junctions and admittances of each subcell are electrically (and optically) coupled, so that the response of the MJSC to a change in electrical bias (either modulated or transient) has to be properly analysed in order to separate the contribution of each subcell. Interestingly, while MJSCs have become one of the main target in photovoltaics, only very few studies can be found in the literature that aim at developing methods to separate the admittance (and thus the capacitance) of each subcell from the measurement performed on the MJSC [32–35].

In a previous study, a method was proposed to separate the capacitance contributions of each subcell within a TSC for the analysis of the capacitance-voltage technique, in order to access the doping densities in the bases and the diffusion potential of each subcell independently [35].

In this article, on account of numerical modelling we demonstrate that this method can be extended to the AS and DLTS characterisation techniques. As an example, we take a III-V/Si TSC in which defects are introduced. First, the AS and DLTS results of the isolated subcells are described and modelled. Then, we discuss the AS and DLTS results modelled from the entire TSC in the dark in order to understand how the

---

electrical coupling complicates the analysis of the results. Next, the proposed method for separating the contributions of each subcell is presented in more detail. Finally, information about the defects present in each subcell of the modelled TSC is extracted by combining the proposed method with the AS and the DLTS characterisation techniques.

2. Background

In this part, we give some theoretical reminders of the main capacitive effects in semiconductor devices as well as some details on the principles of DLTS and AS techniques before presenting the modelled structure.

2.1. Contributions to the admittance in a PN junction

When applying a small AC voltage bias signal at a given angular frequency, ω, one can measure the AC current and deduce the complex admittance, $Y = G + jC\omega$, the real part being the conductance G and the imaginary part the susceptance $jC\omega$, j being the complex number such that $j^2 = -1$ and C the parallel capacitance. There are several contributions to the admittance of a PN junction.

First, the presence of a depletion zone at the junction between the N and P regions causes a so-called depletion-layer capacitance C_w[36],:

$$C_w = \frac{\varepsilon}{w} \qquad (1)$$

w being to the width of the depletion layer and ε the dielectric permittivity of the material. In the absence of deep-level defects, the width of the depletion layer only depends on the built-in potential and on the doping densities in both N and P regions. However, in the presence of deep-level defects in the bandgap of the material, w will also depend on the defect concentrations. In addition, the capture and emission of carriers by the defects can also contribute to the capacitance of the PN junction. When applying a small AC voltage bias signal to measure the admittance of a junction, two charge disturbances occur and contribute to the measured admittance: one due to the modulation of the depletion width and another due to the variation of the occupation of the defects. This latter disturbance depends on the response time of the defect related to emission and capture of free carriers, τ_T, and on the pulsation, ω, of the small AC bias signal. It has been shown that the junction conductance, G_J, and the junction capacitance, C_J, in the presence of defects can then be written [37–39]:

$$\frac{G_J}{\omega} = \Delta C \frac{\omega \tau_T}{1 + \omega^2 \tau_T^2} \qquad (2)$$

and

$$C_J = \frac{\varepsilon}{w} + \frac{\Delta C}{1 + \omega^2 \tau_T^2} \qquad (3)$$

with ΔC the contribution of the defects due to the variation of their occupation under quasi-static conditions ($\omega \tau_T \ll 1$).

Second, the diffusion of free charge carriers across the junction causes a so-called diffusion admittance of which the real part is the diffusion conductance, G_D, and the imaginary part is the diffusion susceptance, $j\omega C_D$, C_D being the diffusion capacitance. Sze calculated G_D and C_D for a PN junction with semi-infinite materials, and he showed that both are related to the dark current density, J_{dark} [36]. This can be extended in the case of solar cells based on an asymmetric junction where the doping concentration of the emitter is much larger than that of the base, introducing an effective lifetime of minority carriers in the base, τ_{eff}, with the approximate expressions:

$$G_D = \frac{dJ_{dark}}{dV} \sqrt{1 + \omega \tau_{eff}} \qquad (4)$$

and

$$C_D = \frac{dJ_{dark}}{dV} \times \frac{\tau_{eff}}{\sqrt{1 + \omega \tau_{eff}}} \qquad (5)$$

with V the applied DC voltage. Note that when $\omega \tau_{eff} \ll 1$, one can rewrite Eq. (4) and Eq. (5) as the low-frequency diffusion conductance ($G_{D,LF}$) and the low-frequency diffusion capacitance ($C_{D,LF}$):

$$G_{D,LF} = \frac{dJ_{dark}}{dV} \qquad (6)$$

and

$$C_{D,LF} = \frac{dJ_{dark}}{dV} \times \tau_{eff} \qquad (7)$$

Usually, the diffusion capacitance is considered in forward bias where it becomes important due to the exponential increase with DC bias, However, it exists whatever the bias and, depending on material parameters, it cannot always be neglected even at zero or reverse bias. The overall capacitance of the PN junction can be written:

$$C = C_J + C_D \qquad (8)$$

Finally, the presence of a strong inversion layer at the interface of a PN junction can create a so-called inversion-layer capacitance. Under certain conditions, this phenomenon can impact the junction admittance especially for heterojunctions, and care has to be taken when analyzing the admittance measurements of such devices [42]. However, this phenomenon has little impact on the electrical coupling between the subcells of the MJSC. Therefore, to simplify this study which aims at developing a method to overcome this coupling, the inversion-layer capacitance will not be considered in the following.

2.2. Admittance spectroscopy (AS)

The AS characterisation technique consists in measuring the admittance of the junction while varying the frequency of the small AC bias excitation and the sample temperature. As shown in the previous section, defects can contribute to the junction admittance and one can thus exploit the temperature and/or the frequency dependence of either the conductance, $G(f, T)$, or the capacitance, $C(f, T)$, to deduce the position of defect energy levels in the bandgap of the base material. In practice however, the contribution of defects to the conductance is often masked by the diffusion conductance and by a parasitic parallel conductance (related to shunts) not taken into account in our analysis and which does not affect the capacitance. Therefore, we will focus in the following on the capacitance only. From Eq. (3) one can deduce that the $C(f)$ curve will follow an inflexion point at a frequency, f_i:

$$f_i = \frac{1}{2\pi \tau_T} \qquad (9)$$

If we consider for example an electron trap (basically a trap located above midgap), it has been shown that the change of occupancy of such defect is significant when its energy crosses or is close to the electron quasi-Fermi level. At this point, the time response of the defect can be written [8–10,38]:

$$\tau_T = \frac{1}{2e_n} \qquad (10)$$

with e_n the emission frequency of the defect to the conduction band, which depends on the difference between the energy position of the defect, E_T, and the energy of the receiving band, E_C, defined as the activation energy, $E_a(E_T) = E_C - E_T$ [8–10,37–41]:

$$e_n(E_T) = \sigma_n v_{th,n} N_C e^{\frac{-E_a(E_T)}{k_B T}} \qquad (11)$$

with σ_n the capture cross section of electrons, $v_{th,n}$ the thermal velocity of electrons, N_C the effective density of states in the conduction band. For a

hole trap, there are similar relations with hole parameters instead of electron ones, and $E_a(E_T) = E_T - E_V$ and E_V the top of the valence band. By increasing the temperature of the sample, the emission rate of the electrons is modified, and the inflexion point of the $C(f)$ curve occurs at a higher frequency. By representing the frequencies of the inflexion points for several temperatures in an Arrhenius plot, one can deduce the activation energy of the defect.

2.3. Deep-Level Transient Spectroscopy (DLTS)

There is a large number of modified techniques to perform Deep-Level Transient Spectroscopy [41]. The classical DLTS characterisation technique proposed by D.V. Lang and considered in this study consists in observing the transient evolution of the capacitance of a junction for several temperatures, after having applied a positive voltage pulse (called filling pulse) to deduce the energy level of the defect in the bandgap of the material, the defect concentration and its capture cross section [8].

Generally, the sample is initially set under zero or reverse bias. The pulse amplitude is chosen so that the junction is momentarily put under more positive bias to inject carriers into the depletion zone. Thus, the probability of occupation changes: the electron traps in the depletion zone are filled with electrons while the hole traps are filled with holes. After the pulse, when the junction is again set under the initial bias, the captured charges are emitted and thus the capacitance exhibits a transient and reaches its steady state value after a certain time related to τ_T. The variation of the capacitance after the pulse can be written [8,41]:

$$\Delta C = \Delta C_0 \times e^{-t/\tau_T} \tag{12}$$

with ΔC_0 the variation of the capacitance just after the pulse.

In the so-called and widely used boxcar technique, one measures the capacitance at two distinct times in the transient, t_1 and t_2, at various temperatures. A DLTS spectrum, $S(T)$ is then defined as $S(T) = C(t_1, T) - C(t_2, T)$. By varying the temperature of the sample, τ_T is modified. One can show that $S(T)$ is maximum at the temperature T_i where the emission frequency of the trap level coincides with r [8]:

$$r = \frac{\ln(t_1/t_2)}{t_1 - t_2} = e_n(T = T_i) \tag{13}$$

where r is often called the window rate defined by t_1 and t_2. By repeating the measurements for different window rates and tracking the maximum of $S(T)$ one can use an Arrhenius plot to deduce the activation energy of the defect in a similar way as in admittance spectroscopy.

2.4. Presentation of the modelled structure

In this study, we take as an example a III-V/Si TSC. We modelled the subcells independently using a TCAD software (Atlas from Silvaco©). This simulator solves the physical equations governing the electrostatics (Poisson, electro-neutrality) and the transport of electrons and holes (drift-diffusion) self-consistently on a 2D mesh [43]. The Top single cell is an AlGaAs NP junction and the Bottom single cell is a c-Si NP junction as represented in Fig. 1(a) and (d), respectively. Some information about the electrical input parameters of the various materials can be found in the supplementary material. We then implement one single deep-defect state in each cell, the properties of the defects are summarized in Table 1. To form the TSC, the two subcells are electrically connected to
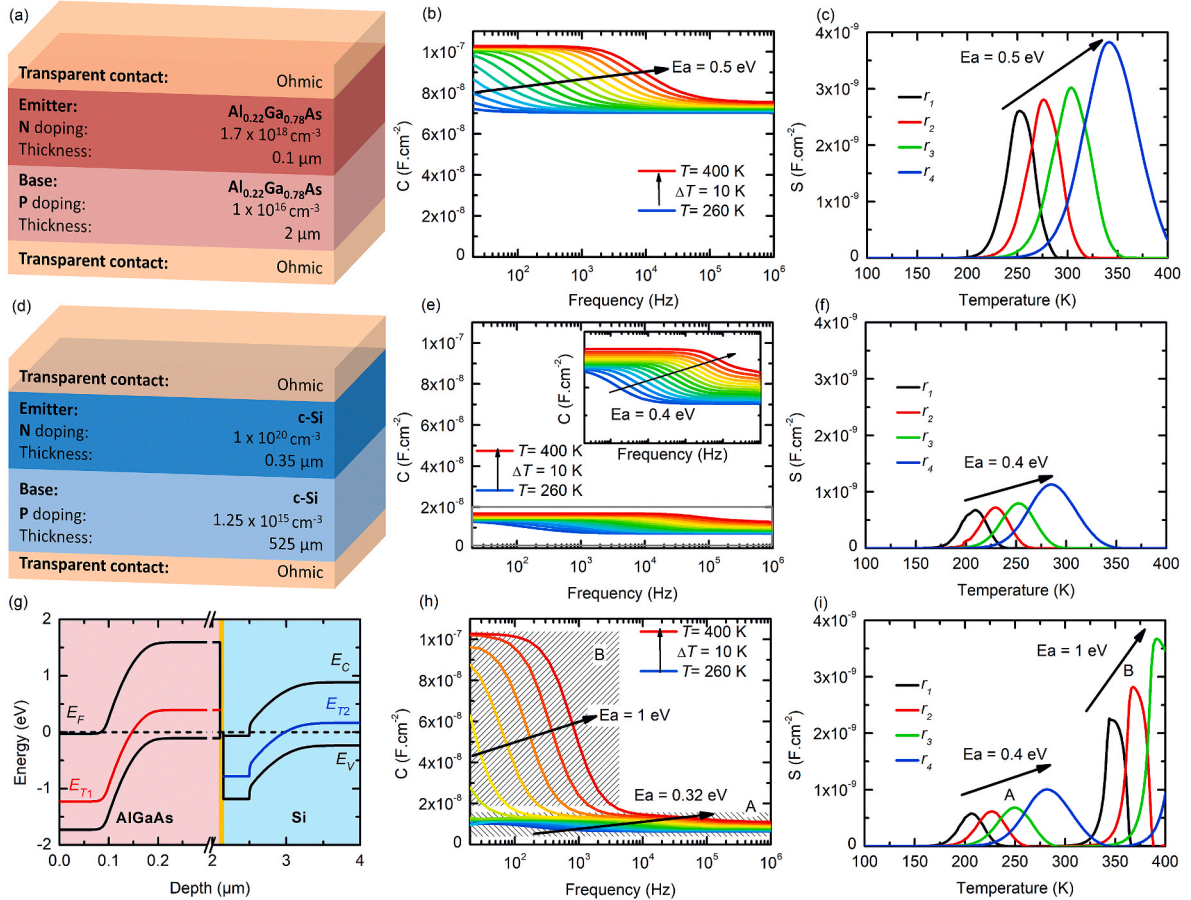

Fig. 1. Modelling results of the Top, Bottom and TSC cells. The top row corresponds to the Top cell: (a) sketch; (b) $C(f, T)$ curves at 0 V DC, and (c) DLTS spectra. The middle row is dedicated to the Bottom cell: (d) sketch; (e) $C(f, T)$ curves at 0 V DC, and (f) DLTS spectra. The bottom row is dedicated to the TSC: (g) energy band diagram; (h) $C(f, T)$ curves at 0 V DC, and (i) DLTS spectra. The regions labelled by the "A" and "B" capital letter are discussed in the text.

Table 1

Properties of the deep defects implemented in the modelling of the Top and Bottom subcells.

Defect properties	Top cell defect	Bottom cell defect
$E_a = E_T - E_V$ (eV)	0.5	0.4
N_T (cm^{-3})	10^{17}	10^{15}
σ_n (cm^2)	10^{-16}	10^{-16}
σ_p (cm^2)	10^{-16}	10^{-16}

each other. In practice, the intermediate layer allowing the transport of charges between the Top and Bottom subcells of a 2T Tandem cell often consists in a tunnel junction. Due to the high doping densities in the layers of the tunnel junction, its capacitance can be neglected when considering the capacitance behavior of a 2T tandem device. In order to greatly simplify the calculations, the tunnel junction is therefore replaced in our models by a perfectly conductive intermediate layer, perfectly transparent and presenting no potential barrier in contact with the Top and Bottom cells. In a previous study, the validity of this simulated structure was experimentally verified by comparing the simulations with admittance measurements performed on a device whose intermediate layer consists in a classical tunnel junction [35].

3. Results and discussions

3.1. Modelling in the dark

In this part, we will start by presenting all the results of the AS and DLTS techniques modelled on the subcells alone and on the TSC in the dark, highlighting the difficulty of extracting defect parameters of the subcells from measurements performed in the dark on the TSC.

3.1.1. AS and DLTS results of the modelled cells

Fig. 1(b) and (e) show the $C(f, T)$ curves of the modelled Top and Bottom single cells, respectively, at 0 V DC when a small AC signal of 20 mV is applied. Fig. 1(c) and (f) represent their respective DLTS spectra deduced from the modelled $C(t, T)$ curves after a filling pulse (from -1 V to 0 V then back to -1 V DC) is applied on the subcells alone. The window rates taken to obtain the DLTS spectra are summarized in Table 2. By extracting the activation energies from the AS and DLTS results of each subcell modelled alone, we successfully find the activation energies of the defects implemented in our simulations.

Then we modelled the TSC by associating the Top and Bottom single cells in series. The band diagram of the TSC is represented in Fig. 1(g). The energy levels of the defects are also represented in Fig. 1(g) (E_{T1} stands for the energy level of the defect in the Top while E_{T2} stands for the one in the Bottom). The modelled $C(f, T)$ curves at 0 V DC are represented in Fig. 1(h) while the DLTS spectra are shown in Fig. 1(i). The AS and DLTS results of the modelled TSC in the dark show two behaviours that could be related to the presence of defects: Fig. 1(h) shows two different regions of inflexions of the $C(f, T)$ curves while we can observe two different regions of peaks in the DLTS spectra (Fig. 1(g)). From the first region, labelled "A", we find an activation energy that is either close (0.32 eV in the AS results) or equal (0.4 eV in the DLTS results) to the signature of the defect in the bottom cell. From the second region of peaks and inflexions, labelled "B", we extract an activation energy of 1 eV which does not correspond to either of the two defects. In the next part, we explain the phenomena responsible for the inflexion points in

Table 2

Window rates used to obtain the DLTS spectra from the $C(t, T)$ curves.

r_1 (s^{-1})	2.6
r_2 (s^{-1})	22.1
r_3 (s^{-1})	117.1
r_4 (s^{-1})	1761.2

the AS results and peaks in the DLTS results in the A and B regions.

3.1.2. Capacitance coupling and filling pulse distribution

Since the two subcells are connected in series, if we call C_1 the capacitance of the Top subcell and C_2 the capacitance of the Bottom subcell, then the capacitance of the TSC, C_{TSC}, should be equal to:

$$C_{TSC} = \left(\frac{1}{C_1} + \frac{1}{C_2} \right)^{-1} \tag{14}$$

In our case, where there is a large difference in doping between the bases of the subcells, one can deduce that the capacitance behavior of the TSC will be close to the behavior of the subcell whose base is the lowest doped. This justifies that the $C(f, T)$ curves in region A in Fig. 1(h) (TSC results) show a similar behavior as in Fig. 1(e) (Bottom cell results). However, because of the capacitance coupling, the two results do not match, and it is not possible to extract with precision the activation energy of the Bottom cell defects from TSC results. More details can be found in the supplementary material section A.

For the DLTS characterisation technique, in addition to the capacitance coupling, one also must consider the distribution of the filling pulse. The two capacitances of the subcells being connected in series, the distribution of the voltage when applying a filling pulse ΔV_{TSC}, is:

$$\begin{cases} \Delta V_1 = \Delta V_{TSC} \times \dfrac{C_2}{C_1 + C_2} \\[2mm] \Delta V_2 = \Delta V_{TSC} \times \dfrac{C_1}{C_1 + C_2} \end{cases} \tag{15}$$

with ΔV_{TSC} the amplitude of the voltage pulse applied on the TSC, ΔV_1 the voltage change in the Top subcell due to the applied pulse, and ΔV_2 the corresponding voltage change in the Bottom subcell. If one makes the assumption that C_1 and C_2 are constant and simply by considering the capacitance ranges ($C_1 \sim 10^{-7}$ F.cm^{-2} and $C_2 \sim 10^{-8}$ F.cm^{-2}), one can deduce that almost 90% of ΔV_{TSC} is actually applied on the Bottom subcell which is confirmed by our modelling (see Fig. S3 from supplementary material section A).

In our case, one can deduce that almost only the defect in the Bottom subcell is probed when performing DLTS on this TSC in the dark. This explains why the activation energy extracted from the A region in Fig. 1(i) is equal to the activation energy of the defect in the Bottom subcell. But this only stands for our particular case. In general, the filling pulse will mostly apply on the subcell with the lowest capacitance, so in the dark, mostly this subcell can eventually be probed by DLTS. But if the two capacitances are in the same range, results will be more difficult to analyse. Moreover, in the following we show that diffusion also plays a role and leads to artefacts regarding defects identification.

3.1.3. Diffusion phenomena

Capacitance coupling and voltage distribution explain well the behavior of the AS and DLTS results in the A region of Fig. 1(h) and (i). Now, to understand the behavior in the B region, we modelled the AS and DLTS curves of the TSC without defect (Fig. 2(a) and (b)). Here, we can see that the defect signatures disappeared. However, the inflexion points in AS and the unusual DLTS peaks observable in the B regions remain but occur at higher temperatures. This means that the inflexions and peaks in the B regions of Fig. 1(h) and (i) are not related to the presence of defects in the structure.

In fact, the increase of the temperature increases the saturation current density in the subcells. This means, based on Eqs. (4) and (5), that the diffusion capacitance and the diffusion conductance also increase with the temperature. In the case of subcell with high effective lifetime material such as our c-Si Bottom subcell, diffusion capacitance and diffusion conductance cannot be neglected at high temperature. This is verified indeed in the Bottom c-Si subcell as shown in Fig. 3 where the real part of the admittance surpasses its imaginary part above 375 K.
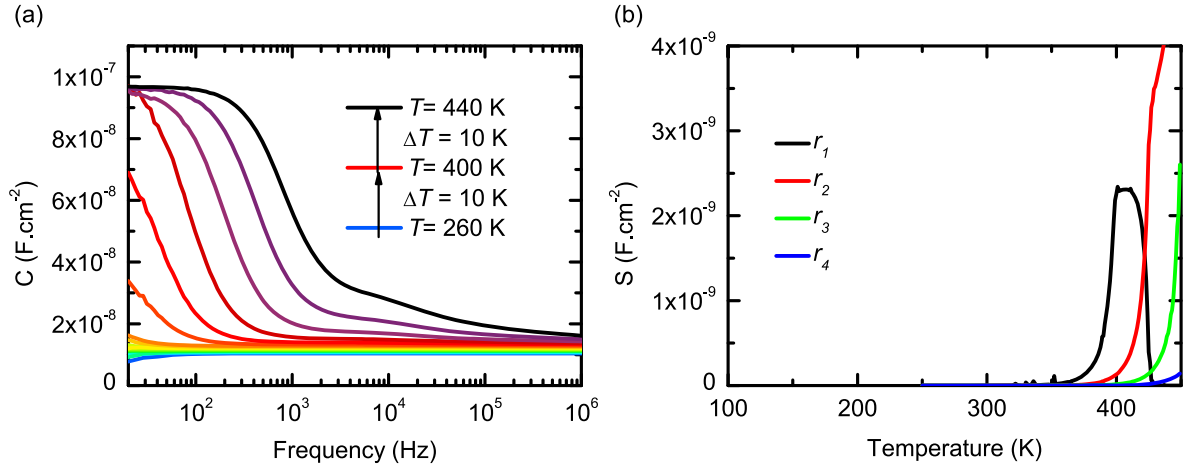
Fig. 2. (a) AS and (b) DLTS results of the TSC modelled in the dark without defect.
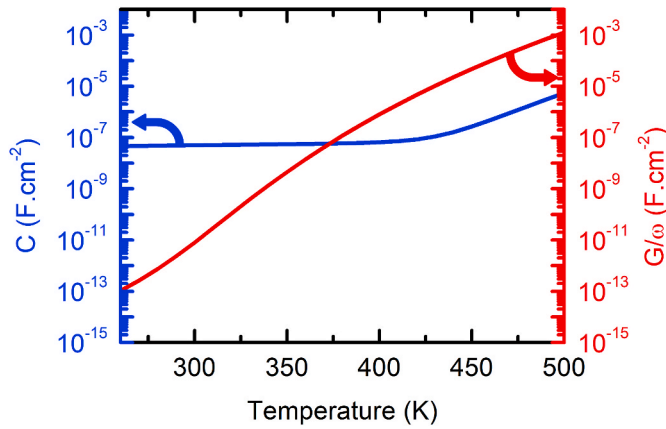

Fig. 3. Temperature dependence of the low-frequency capacitance and the low-frequency conductance divided by the pulsation of the small AC signal (at 20 Hz) in the modelled c-Si Bottom subcell without defect.

Consequently, we must consider the diffusion conductance and the diffusion capacitance of the Bottom subcell to explain our results at high temperature. We note $C_{w,1}$ the depletion-layer capacitance of the Top subcell, $C_{w,2}$, $C_{D,2}$ and $G_{D,2}$, the depletion-layer capacitance, diffusion capacitance and diffusion conductance of the Bottom subcell, respectively. The equivalent circuit of the TSC is now represented in Fig. 4.
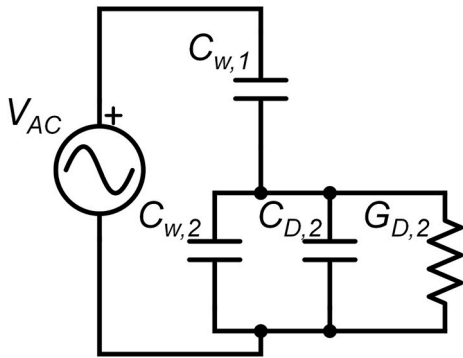

Fig. 4. Simplified AC circuit of the TSC if we consider the contribution of diffusion phenomena in the bottom subcell. $C_{w,1}$ is the depletion-layer capacitance of the Top subcell, $C_{w,2}$, $C_{D,2}$ and $G_{D,2}$ are the depletion-layer capacitance, diffusion capacitance and diffusion conductance of the Bottom subcell, respectively.

The total capacitance of the Top subcell, C_1 is equal to $C_{w,1}$; the total capacitance of the Bottom subcell, C_2 is equal to $C_{w,2} + C_{D,2}$; the total conductance of the Bottom subcell, G_2 is equal to $G_{D,2}$. Therefore, the equivalent capacitance of the TSC is now:

$$C_{TSC} = C_1 \times \frac{C_2}{C_1 + C_2} \times \frac{\omega^2 + \left(\frac{G_2}{C_2}\right)^2 \times \frac{C_2}{C_1 + C_2}}{\omega^2 + \left(\frac{G_2}{C_2}\right)^2 \times \left(\frac{C_2}{C_1 + C_2}\right)^2} \quad (16)$$

Based on this equation, one can deduce that the evolution of C_{TSC} with frequency will follow a first inflexion at a point where $\omega = \omega_{Sh} = \frac{G_2}{\sqrt{3}(C_1 + C_2)}$. For lower frequencies, C_{TSC} tends toward C_1 (the bottom subcell is shunted) and for higher frequencies, C_{TSC} tends toward $(1/C_1 + 1/C_2)^{-1}$ as it can be seen in Fig. 5(a). A second decrease occurs when the diffusion capacitance in the Bottom subcell decreases with increasing frequency (see Eq. (5)) and the position of this inflexion is noted ω_{HF}.

Considering the diffusion phenomena in the Bottom subcell, the distribution of the voltage in the structure is modified:

$$\begin{cases} \Delta V_1 = \Delta V_{TSC} \times \dfrac{\dfrac{1}{j\omega C_1}}{\dfrac{1}{j\omega C_2 + G_2} + \dfrac{1}{j\omega C_1}} \\[3ex] \Delta V_2 = \Delta V_{TSC} \times \dfrac{\dfrac{1}{j\omega C_2 + G_2}}{\dfrac{1}{j\omega C_2 + G_2} + \dfrac{1}{j\omega C_1}} \end{cases} \quad (17)$$

By assuming constant values of C_1, C_2 and G_2 we can obtain the expression of the voltage distribution in the subcells versus time after the filling pulse by writing Eq. (17) in the Laplace domain, then by applying inverse Laplace transform:

$$\begin{cases} \Delta V_1 = \Delta V_{TSC} \times \left(1 - \dfrac{C_1}{C_1 + C_2} e^{-t\frac{G_2}{C_1 + C_2}}\right) \\[3ex] \Delta V_2 = \Delta V_{TSC} \times \dfrac{C_1}{C_1 + C_2} e^{-t\frac{G_2}{C_1 + C_2}} \end{cases} \quad (18)$$

This equation well describes the voltage distribution in our modelling (Fig. 5 (c)). Just before the end of the pulse, V_1 and V_2 are equal to zero. At $t = 0$, when $\Delta V_{TSC} = -1$ V, simply by considering the capacitance ranges and Eq. (18), one can deduce that almost 90% of ΔV_{TSC} is actually applied on the Bottom subcell. But as t increases, V_2 tends to reach back its initial value ($\Delta V_2 \rightarrow 0$) while all the pulse amplitude is applied on V_1 ($\Delta V_1 \rightarrow \Delta V_{TSC}$). However, in our modelling, we can see that the evolution of the voltage distribution is indeed
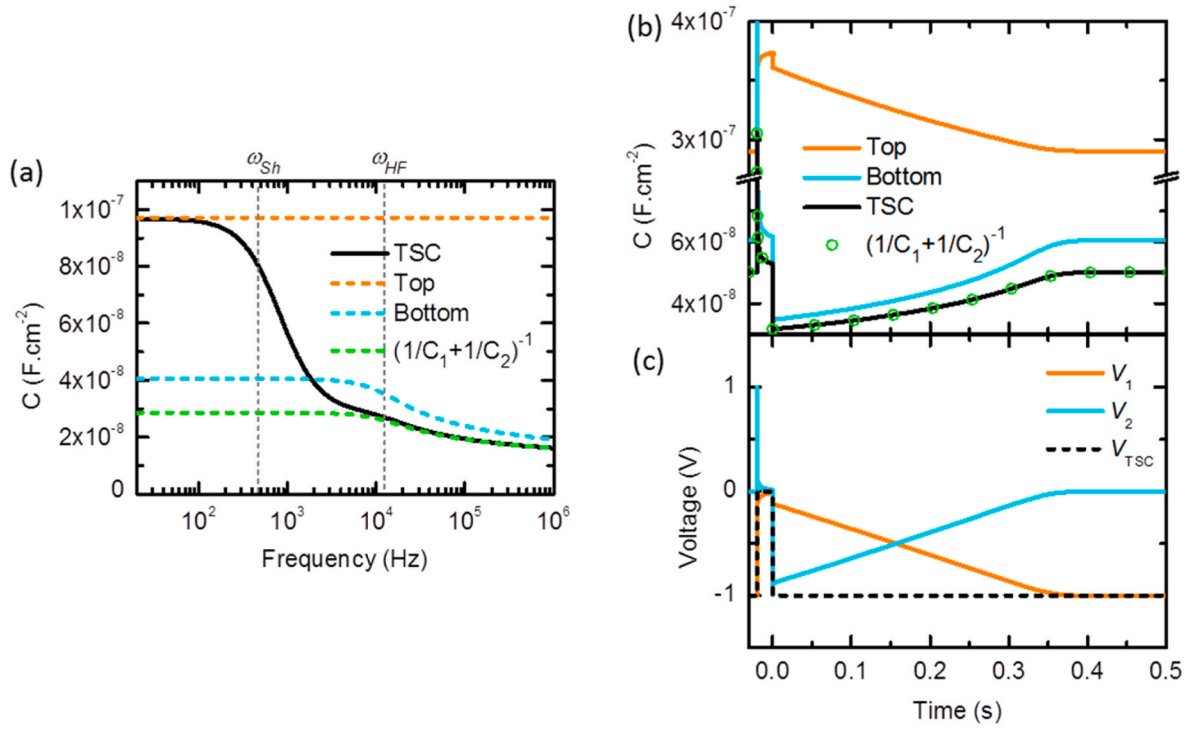
Fig. 5. (a) $C(f)$ curve modelled at 0 V DC and 440 K of the TSC, the Top and the Bottom subcells without defect, compared with the $(1/C_1 + 1/C_2)^{-1}$ values; (b) $C(t)$ curve modelled at 390 K of the TSC, the Top and the Bottom subcells without defect, compared with the $(1/C_1 + 1/C_2)^{-1}$ value after the filling pulse; (c) The evolution of the voltage distribution between the subcells of the TSC without defect.

exponential when the filling pulse is applied but not after it ended. This could be explained by resistive effects or because we assumed C_1, C_2 and G_2 as constant while they are actually voltage dependent and thus evolve with time as can be seen on Fig. 5(b) [44]. This also induces a variation of C_{TSC} after the pulse (Fig. 5(b)) which could be mis-interpreted as the consequence of a defect. From Eq. (18), we can notice that the characteristic time of the evolution of the voltage is $\frac{C_1+C_2}{G_2}$, and will be noted t_{Sh} to refer to ω_{Sh}.

When increasing the temperature of the sample, the diffusion phe-nomena are more important and thus change the values of ω_{Sh} and t_{Sh}. ω_{Sh} increases while t_{Sh} decreases with increasing temperature which lead to the inflexions and peaks that can be seen in the B region of Fig. 1 (h) and (i). In fact, we can assume that the dependence of ω_{Sh} and t_{Sh} on temperature follows the dependence of G_2 which is proportional to the dark current density of the silicon subcell. In first approximation this is proportional to n_i^2, n_i being the intrinsic carrier concentration given by:

$$n_i = \sqrt{N_C N_V} \times e^{-E_g/2k_BT} \tag{19}$$

with E_g the gap of the material, N_V and N_C the effective density of states in the valence and conduction bands, respectively.

This can explain the activation energy of $\approx$1 eV extracted from the Arrhenius plot of the inflexions and peaks in the B region of Fig. 1(h) and (i) that reflect the bandgap energy of the silicon material.

To conclude this part, utilizing AS and DLTS characterisation tech-niques on the TSC in the dark can lead to misinterpretation of the results. First, due to the electrical coupling, the defects signatures are mixed. If the capacitance of one of the subcells is important enough, then only the defect signatures of the other subcell might be observable but due to the coupling, the extraction of their properties might lead to errors. Regarding the DLTS characterisation technique, additional consider-ation should be given to the distribution of the filling pulse applied on the structure. If, as it is the case in this study, the filling pulse is mostly applied on one of the two subcells, then only this one is probed. Second, the impact of the diffusion phenomena can be mixed with the signature

of a defect or can lead to an AS and DLTS signature that can be improperly attributed to the existence of a defect that does not exist. The impact of those phenomena and of the capacitance- and voltage coupling strongly depend on the studied structure. Each technology might behave differently. Therefore, in the dark, it seems very difficult to properly analyse AS or DLTS results without a strong support from complementary modelling.

In the following, we propose a simple and non-destructive method allowing (i) to decouple the capacitances, (ii) to know and control how the voltage is shared between the subcells, (iii) to know which subcell is probed and (iv) to ensure that the diffusion phenomena cannot be confused with the defect signatures anymore.

3.2. Proposed light bias method

3.2.1. Overcoming the electrical coupling: use of light biases

The proposed method uses a light bias whose wavelength is such that it can be absorbed only by one of the subcells in the TSC. This results in fixing the polarization of the absorbing subcell near its open-circuit voltage if the applied voltage on the TSC is reverse or slightly direct (below the open-circuit voltage value of the absorbing subcell). In that way we can control in which subcell the diffusion phenomena are important since those mostly occur in the direct polarized subcell, i.e. the absorbing subcell. More details can be found in Refs. [35,44]. We use K as the index of the subcell in the dark and L as the index of the other subcell that absorbs the light. Then, Eqs. (16) and (18) become:

$$C_{TSC} = C_K \times \frac{C_L}{C_K+C_L} \times \frac{\omega^2 + \left(\frac{G_L}{C_L}\right)^2 \times \frac{C_L}{C_K+C_L}}{\omega^2 + \left(\frac{G_L}{C_L}\right)^2 \times \left(\frac{C_L}{C_K+C_L}\right)^2} \tag{20}$$

and

$$\begin{cases} \Delta V_L = \Delta V_{TSC} \times \dfrac{C_K}{C_K + C_L} e^{-t\frac{G_L}{C_K+C_L}} \\ \Delta V_K = \Delta V_{TSC} \times \left(1 - \dfrac{C_K}{C_K + C_L} e^{-t\frac{G_L}{C_K+C_L}}\right) \end{cases} \tag{21}$$

Also, ω_{Sh} becomes $\frac{G_L}{\sqrt{3}(C_K+C_L)}$ and t_{Sh} becomes $\frac{C_K+C_L}{G_L}$.

First, from Eq. (20), we can deduce that for $\omega < \omega_{Sh}$, C_{TSC} tends toward C_K. Unlike the case of the TSC in the dark, here we can choose which subcell is shunted at low frequency and only obtain the capacitance of the subcell in the dark by adapting the wavelength of the light bias. For example, with a 405 nm light bias fully absorbed in the Top subcell (this case is referred to as TSC$_{405}$), for pulsation below ω_{Sh} one can probe only the Bottom subcell (see Fig. 6(a)) while with a 980 nm light bias fully absorbed in the Bottom subcell (this case is referred to as TSC$_{980}$), one can probe only the Top subcell (see Fig. 6(b)). Second, since the absorbing subcell is polarized in direct while the other subcell is polarized in reverse, we know that $C_L \gg C_K$. Based on Eq. (21), we can assume that when a voltage step is applied on the TSC, only a little fraction of it will occur in the absorbing subcell. For example, in the TSC$_{405}$ case, the filling pulse applied on the TSC mostly occurs in the Bottom subcell (see Fig. 7(a)) while the Top subcell is polarized at its open-circuit voltage value. In the opposite, in the TSC$_{980}$ case, the filling pulse applied on the TSC mostly occurs in the Top subcell (see Fig. 7(b)) while the Bottom subcell is polarized at its open-circuit voltage value.

This method allows to choose which subcell is probed. However, there are still inflexions in the $C(f)$ curves and transient evolutions of the voltage distribution. In the previous section, we have shown that in the dark, the position of the inflexions and the characteristic times of the transient evolution are temperature dependent and disturb the observation of the defect signatures. Thus, in the following, we are going to demonstrate that when the TSC is under specific illumination, ω_{Sh} and t_{Sh} can be easily distinguished from the defect signatures.

3.2.2. Distinguishing the defects signatures from diffusion phenomena

Unlike the case were the TSC is in the dark, when one of the two subcells fully absorbs the light, the modelling shows negligible dependency of ω_{Sh} and t_{Sh} with temperature (see supplementary material section B). In fact, when the DC voltage applied on the TSC is reverse or zero and when one of the two subcells absorbs the light, the current flowing through the TSC is close to zero. This implies that within the absorbing subcell, the photogenerated current, J_{ph}, is compensated by the dark current density ($J_{ph} = J_{dark}$). Eqs. (4) and (5) become:

$$G_D = \frac{qJ_{ph}}{k_B T} \sqrt{1 + \omega\tau_{eff}} \tag{22}$$

and

$$C_D = \frac{qJ_{ph}}{k_B T} \times \frac{\tau_{eff}}{\sqrt{1 + \omega\tau_{eff}}} \tag{23}$$

The photogenerated current being, at first order, independent of the temperature, it means that under such illumination condition, the temperature dependence of the diffusion capacitance and conductance can be neglected as well as the temperature dependence of ω_{Sh} and t_{Sh}. (see Fig. S4 and Fig. S5 from supplementary material section B).

On another hand, this also means that we can tune their values by changing the intensity of the light biases to modify the value of the photogenerated current in the absorbing subcell. By choosing a photon flux important enough, one can shift ω_{Sh} toward high frequency such as one can observe the AS results of the subcell in the dark over the entire considered frequency range. Also, one can decrease t_{Sh} so that it is outside the time windows considered when performing DLTS analyses and one can thus observe the defect signature of the subcell in the dark. More details can be found in the supplementary material.

3.2.3. AS and DLTS combined with light biases: extracting the defect properties of each subcell

On Fig. 8(b) and (d), we represent the modelled $C(f,T)$ curves and DLTS spectra of the TSC$_{405}$ under an illumination of 1 W cm^{-2} (high enough such that ω_{Sh} is outside the considered frequency range and t_{Sh} is outside the time windows used for DLTS analysis). In order to compare the AS and DLTS results of the TSC$_{405}$ with those of the Bottom subcell alone (Fig. 8(a) and (c)), we make sure that they are in the same polarization conditions. We have shown that in order to do so, one needs to add the open-circuit voltage of the Top subcell to the polarization of the TSC$_{405}$ [35].

In both AS and DLTS, we notice that, we obtain exactly the same figures whether the modelling was carried out on the Bottom cell alone or on the TSC$_{405}$. The same activation energy can be extracted in both cases and corresponds to the activation energy of the defect implemented in our modelling. The inflexion points and the unusual DLTS peaks observable in the B region of the modelling results in the dark are not observable when the TSC is under the 405 nm light bias as previously discussed in Section 3.2.2 so that only the signature of the defect in the subcell in the dark can be seen.

The same analysis can be done with Fig. 9 where we compare the $C(f,T)$ curves and DLTS spectra of the TSC$_{980}$ under an illumination of 1 W cm^{-2} (Fig. 9(b) and (d)) with the AS and DLTS results of the Top subcell alone (Fig. 9(a) and (c)). Under the 980 nm light bias, we can clearly see only the contribution of the defect in the Top subcell which was not observable when the modelling was performed on the TSC in the dark.
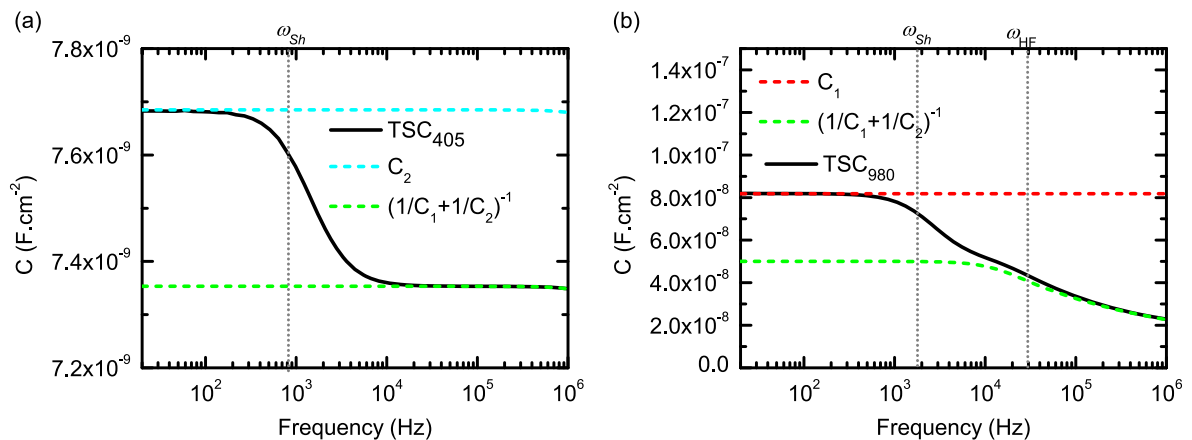

Fig. 6. curves modelled at 300 K from (a) the TSC, the Bottom subcell and $(1/C_1 + 1/C_2)^{-1}$ in the TSC$_{405}$ case without defects under 1 mW cm^{-2} light bias and (b) the TSC, the Top subcell and $(1/C_1 + 1/C_2)^{-1}$ in the TSC$_{980}$ case without defects under 1 mW cm^{-2} light bias.
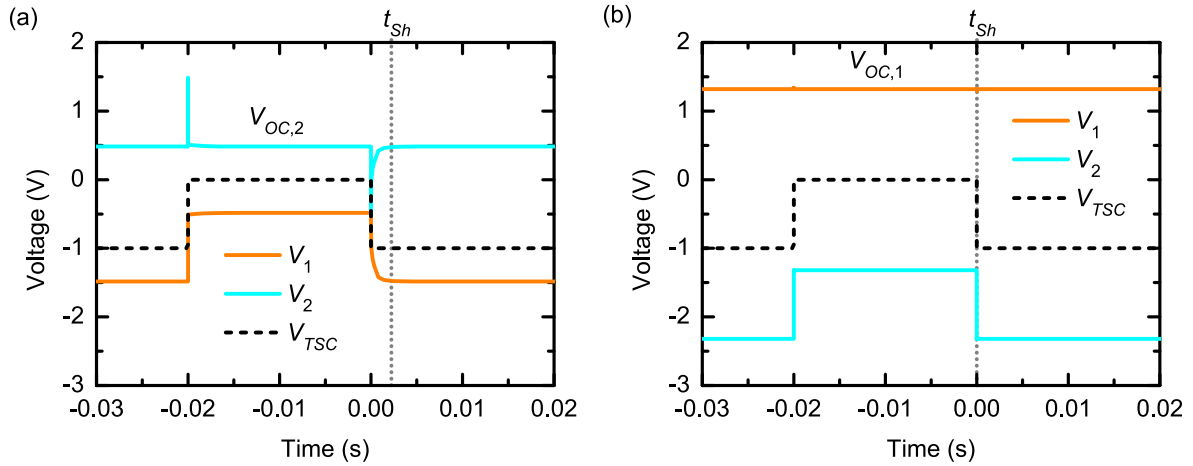
Fig. 7. Distribution of the applied voltage between the subcells versus time (a) in the TSC$_{405}$ case and (b) in the TSC$_{980}$ case at 300 K under 1 W cm^{-2} light bias.
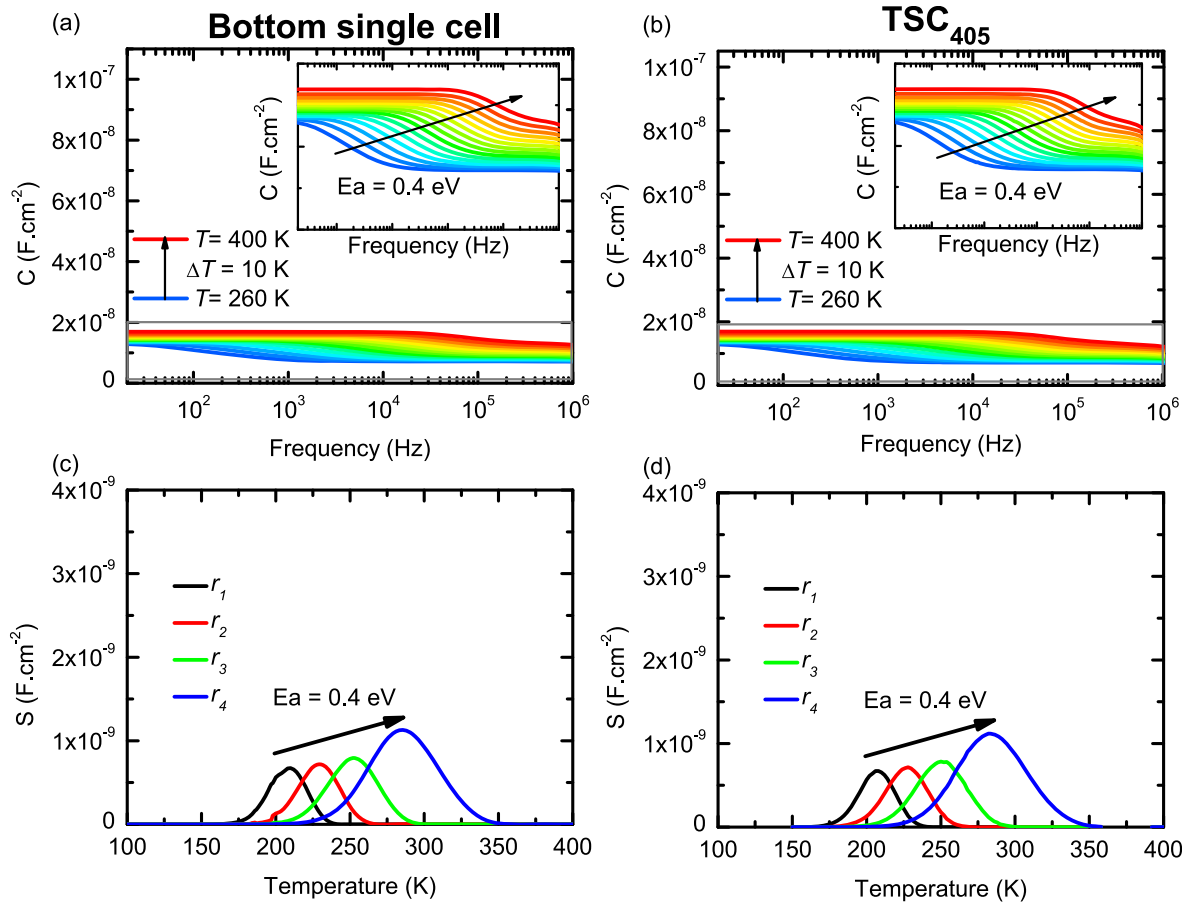

Fig. 8. (a) AS results of the Bottom subcell modelled alone at 0 V DC; (b) AS results of the TSC$_{405}$ under a light power density of 1 W cm^{-2} and polarized at the open-circuit value of the absorbing Top subcell; (c) DLTS results of the Bottom subcell modelled alone; (d) DLTS results of the TSC$_{405}$ under a light power density of 1 W cm^{-2}.

The high frequency drops of the curves in Fig. 9(b) are due to the decrease of the bottom subcell capacitance with increasing frequency. In fact, at such high frequency (compared to the inverse of the effective minority carrier lifetime of the absorbing subcell) the method encounters some limitations. Indeed, the diffusion capacitance and conductance of the absorbing subcell, $C_{D,L}$ and $G_{D,L}$ (Eq. (4) and (5)) become frequency dependent, and so also does ω_{sh}. The capacitances are not decoupled anymore (for frequency higher than 10^4 Hz) but with a photon flux high enough, the capacitance of the absorbing subcell is so

important that it can still be negligible in C_{TSC} until the drop of $C_{D,L}$ with increasing frequency becomes too important (for frequencies higher than 10^5 Hz). When increasing the temperature, this point happens at a slightly lower frequency because of the temperature dependence of $C_{D,L}$.

4. Conclusion

We have described a method to access the defects properties in each subcell within a TSC by combining AS and DLTS characterisation
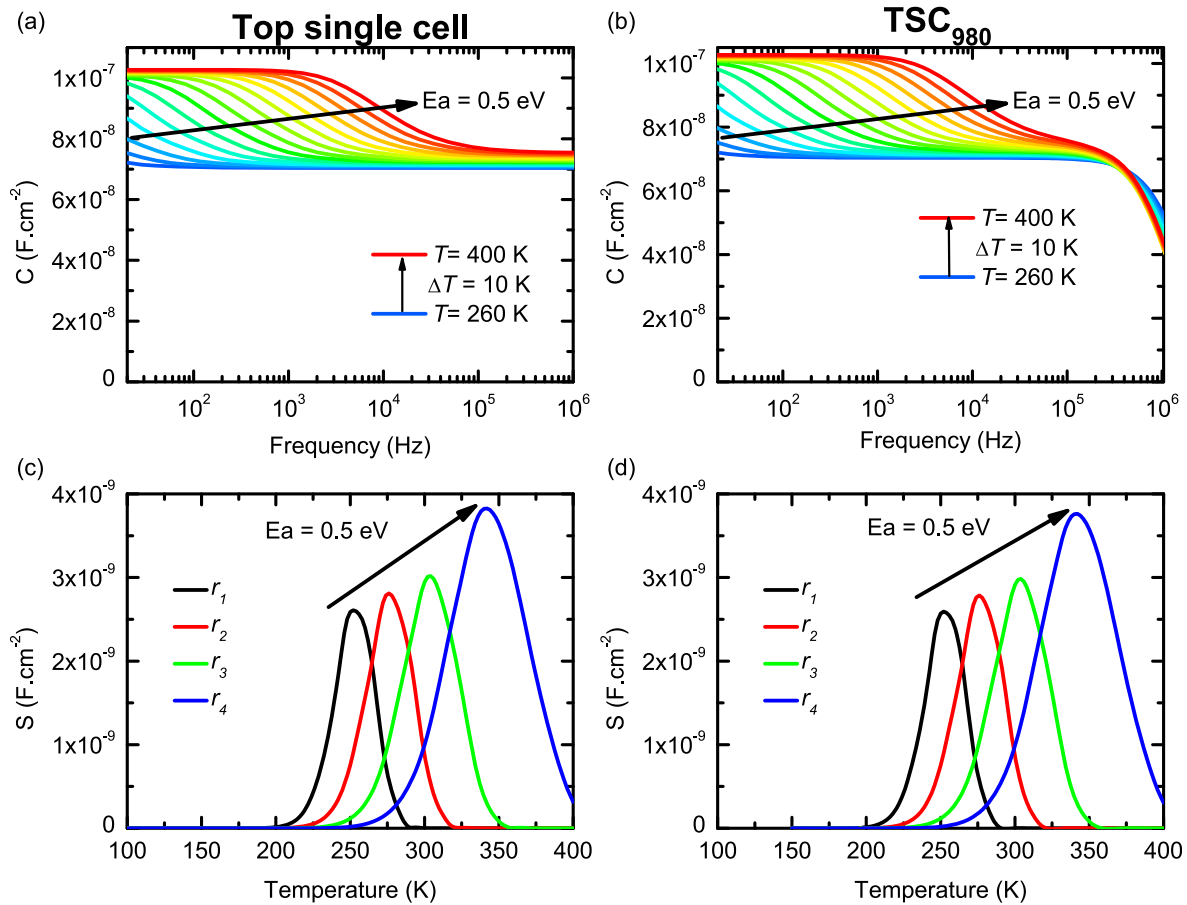
Fig. 9. (a) AS results of the Top subcell modelled alone at 0 V DC; (b) AS results of the TSC$_{980}$ under a light power density of 1 W cm^{-2} and polarized at the open-circuit value of the Bottom subcell; (c) DLTS results of the Top subcell modelled alone; (d) DLTS results of the TSC$_{980}$ under a light power density of 1 W cm^{-2}.

techniques with the use of specific light biases. Without such light biases, if the TSC is in the dark, the defect signatures of each subcell can be coupled and depending on the materials and defect properties, the AS and DLTS signals of one of the subcells can prevail. In addition, it has been shown that the increase of the diffusion phenomena with temperature in one of the subcells can have an impact on the AS and DLTS signals. Very importantly, it can lead to artefacts in AS and DLTS that can be misinterpreted as the signature of a defect.

Using analytical and numerical modelling approaches, we have shown that the use of specific light biases such that the subcell of interest is in the dark while the other fully absorbs the light, allows to "choose" in which subcell the diffusion phenomena mostly occur: the absorbing subcell. This causes the shunt of the capacitance of the absorbing subcell at low frequency and ensures that a filling pulse will be mostly applied in the subcell in the dark. Therefore, the use of light biases allows to choose, both in AS and DLTS characterisation techniques, which subcell is probed. The use of light biases also changes the dependency of the diffusion phenomena with temperature which can be more easily distinguished from the defect signatures. Also, by adjusting the power densities of the light biases the impact of the diffusion phenomena on the AS and DLTS signals can be shifted out of the considered frequency range and time windows such that the obtained signals can be equal to those of the subcells alone. This simple and non-destructive method could easily be extended to MJSCs consisting of more than two subcells by ensuring that each subcell in the MJSC is light-biased, except the one that is to be probed.

CRediT authorship contribution statement

Cyril Leon: Methodology, Software, Validation, Visualization, Writing – original draft, Writing – review & editing, Investigation, Formal analysis. **Sylvain Le Gall:** Writing – review & editing, Validation, Supervision, Project administration, Methodology, Investigation. **Marie-Estelle Gueunier-Farret:** Investigation, Methodology, Project administration, Supervision, Validation, Writing – review & editing. **Jean-Paul Kleider:** Writing – review & editing, Validation, Supervision, Project administration, Methodology, Investigation.

Declaration of competing interest

The authors declare that they have no known competing financial interests or personal relationships that could have appeared to influence the work reported in this paper.

Appendix A. Supplementary data

Supplementary data to this article can be found online at https://doi.org/10.1016/j.solmat.2022.111699.

References

[1] W. Shockley, H.J. Queisser, Detailed balance limit of efficiency of p-n junction solar cells, J. Appl. Phys. 32 (1961) 510, https://doi.org/10.1063/1.1736034.

[2] J.F. Geisz, M.A. Steiner, N. Jain, K.L. Schulte, R.M. France, W.E. McMahon, E. E. Perl, D.J. Friedman, Building a six-junction inverted metamorphic concentrator solar cell, IEEE J. Photovoltaics 8 (2018) 626.

[3] P.T. Chiu, D.C. Law, R.L. Woo, S.B. Singer, D. Bhusari, W.D. Hong, A. Zakaria, J. Boisvert, S. Mesropian, R.R. King, N.H. Karam, 35.8% space and 38.8%

terrestrial 5J direct bonded cells, 2014, IEEE 40th Photovolt. Spec. Conf. PVSC 2014 (2014) 11–13, https://doi.org/10.1109/PVSC.2014.6924957.

[4] K. Sasaki, T. Agui, K. Nakaido, N. Takahashi, R. Onitsuka, T. Takamoto, Development of InGaP/GaAs/InGaAs inverted triple junction concentrator solar cells, AIP Conf. Proc. 1556 (2013) 22, https://doi.org/10.1063/1.4822190.

[5] M.A. Green, E.D. Dunlop, D.H. Levi, J. Hohl-Ebinger, M. Yoshita, A.W.Y. Ho-Baillie, Solar cell efficiency tables (version 54), Prog. Photovoltaics Res. Appl. 27 (2019) 565–575, https://doi.org/10.1002/PIP.3171.

[6] S. Essig, C. Allebé, T. Remo, J.F. Geisz, M.A. Steiner, K. Horowitz, L. Barraud, J. S. Ward, M. Schnabel, A. Descoeudres, D.L. Young, M. Woodhouse, M. Despeisse, C. Ballif, A. Tamboli, Raising the one-sun conversion efficiency of III–V/Si solar cells to 32.8% for two junctions and 35.9% for three junctions, Nat. Energy 29 (2017) (2017) 1–9, https://doi.org/10.1038/nenergy.2017.144, 2.

[7] M. Meusel, C. Baur, G. Siefer, F. Dimroth, A.W. Bett, W. Warta, Characterization of monolithic III–V multi-junction solar cells—challenges and application, Sol. Energy Mater. Sol. Cells 90 (2006) 3268–3275, https://doi.org/10.1016/J.SOLMAT.2006.06.025.

[8] D.V. Lang, Deep-level transient spectroscopy: a new method to characterize traps in semiconductors, J. Appl. Phys. 45 (1974) 3023, https://doi.org/10.1063/1.1663719.

[9] D.L. Losee, Admittance spectroscopy of deep impurity levels: ZnTe Schottky barriers, Appl. Phys. Lett. 21 (1972) 54, https://doi.org/10.1063/1.1654276.

[10] D.L. Losee, Admittance spectroscopy of impurity levels in Schottky barriers, J. Appl. Phys. 46 (1975) 2204, https://doi.org/10.1063/1.321865.

[11] A. Ali, T. Gouveas, M.A. Hasan, S.H. Zaidi, M. Asghar, Influence of deep level defects on the performance of crystalline silicon solar cells: experimental and simulation study, Sol. Energy Mater. Sol. Cells 95 (2011) 2805–2810, https://doi.org/10.1016/j.solmat.2011.05.032.

[12] A.I. Baranov, A.S. Gudovskikh, A.Y. Egorov, D.A. Kudryashov, S. Le Gall, J. P. Kleider, Defect properties of solar cells with layers of GaP based dilute nitrides grown by molecular beam epitaxy, J. Appl. Phys. 128 (2020), 023105, https://doi.org/10.1063/1.5134681.

[13] A.I. Baranov, A.S. Gudovskikh, D.A. Kudryashov, A.A. Lazarenko, I.A. Morozov, A. M. Mozharov, E.V. Nikitina, E.V. Pirogov, M.S. Sobolev, K.S. Zelentsov, A. Y. Egorov, A. Darga, S. Le Gall, J.P. Kleider, Defect properties of InGaAsN layers grown as sub-monolayer digital alloys by molecular beam epitaxy, J. Appl. Phys. 123 (2018) 161418, https://doi.org/10.1063/1.5011371.

[14] M. Burgelman, P. Nollet, Admittance spectroscopy of thin film solar cells, Solid State Ionics 176 (2005) 2171–2175, https://doi.org/10.1016/j.ssi.2004.08.048.

[15] J. Chantana, D. Hironiwa, T. Watanabe, S. Teraji, T. Minemoto, Flexible Cu(In,Ga) Se-2 solar cell on stainless steel substrate deposited by multi-layer precursor method: its photovoltaic performance and deep-level defects, Prog. Photovoltaics Res. Appl. 24 (2016) 990–1000, https://doi.org/10.1002/pip.2748.

[16] Y.C. Choi, D.U. Lee, J.H. Noh, E.K. Kim, S. Il Seok, Highly improved Sb2S3 sensitized-inorganic-organic heterojunction solar cells and quantification of traps by deep-level transient spectroscopy, Adv. Funct. Mater. 24 (2014) 3587–3592, https://doi.org/10.1002/adfm.201304238.

[17] Z. Djebbour, A. Darga, A. Migan Dubois, D. Mencaraglia, N. Naghavi, J. F. Guillemoles, D. Lincot, Admittance spectroscopy of cadmium free CIGS solar cells heterointerfaces, Thin Solid Films 511–512 (2006) 320–324, https://doi.org/10.1016/j.tsf.2005.11.087.

[18] T. Eisenbarth, T. Unold, R. Caballero, C.A. Kaufmann, H.W. Schock, Interpretation of admittance, capacitance-voltage, and current-voltage signatures in Cu(In,Ga)Se2 thin film solar cells, J. Appl. Phys. 107 (2010) 0–12, https://doi.org/10.1063/1.3277043.

[19] M. González, A.M. Carlin, C.L. Dohrman, E.A. Fitzgerald, S.A. Ringel, Determination of bandgap states in p-type In0.49Ga 0.51P grown on SiGe/Si and GaAs by deep level optical spectroscopy and deep level transient spectroscopy, J. Appl. Phys. 109 (2011) 0–7, https://doi.org/10.1063/1.3559739.

[20] A.S. Gudovskikh, J.P. Kleider, R. Chouffot, N.A. Kalyuzhnyy, S.A. Mintairov, V. M. Lantratov, III-phosphides heterojunction solar cell interface properties from admittance spectroscopy, J. Phys. D Appl. Phys. 42 (2009) 165307, https://doi.org/10.1088/0022-3727/42/16/165307.

[21] A.S. Gudovskikh, J.P. Kleider, J. Damon-Lacoste, P. Roca i Cabarrocas, Y. Veschetti, J.C. Muller, P.J. Ribeyron, E. Rolland, Interface properties of a-Si:H/c-Si heterojunction solar cells from admittance spectroscopy, Thin Solid Films 511–512 (2006) 385–389, https://doi.org/10.1016/j.tsf.2005.12.111.

[22] S. Heo, G. Seo, Y. Lee, D. Lee, M. Seol, J. Lee, J.B. Park, K. Kim, D.J. Yun, Y.S. Kim, J.K. Shin, T.K. Ahn, M.K. Nazeeruddin, Deep level trapped defect analysis in CH3NH3PbI3 perovskite solar cells by deep level transient spectroscopy, Energy Environ. Sci. 10 (2017) 1128–1133, https://doi.org/10.1039/c7ee00303j.

[23] X. Hu, J. Tao, G. Weng, J. Jiang, S. Chen, Z. Zhu, J. Chu, Investigation of electrically-active defects in Sb2Se3 thin-film solar cells with up to 5.91%

efficiency via admittance spectroscopy, Sol. Energy Mater. Sol. Cells 186 (2018) 324–329, https://doi.org/10.1016/j.solmat.2018.07.004.

[24] M. Jiang, F. Lan, B. Zhao, Q. Tao, J. Wu, D. Gao, G. Li, Observation of lower defect density in CH3NH3Pb(I,Cl)3 solar cells by admittance spectroscopy, Appl. Phys. Lett. 108 (2016) 243505, https://doi.org/10.1063/1.4953834.

[25] J. Lauwaert, L. Van Puyvelde, J. Lauwaert, J.W. Thybaut, S. Khelifi, M. Burgelman, F. Pianezzi, A.N. Tiwari, H. Vrielinck, Assignment of capacitance spectroscopy signals of CIGS solar cells to effects of non-ohmic contacts, Sol. Energy Mater. Sol. Cells 112 (2013) 78–83, https://doi.org/10.1016/J.SOLMAT.2013.01.014.

[26] H.S. Lee, M. Yamaguchi, N.J. Ekins-Daukes, A. Khan, T. Takamoto, T. Agui, K. Kamimura, M. Kaneiwa, M. Imaizumi, T. Ohshima, H. Itoh, Deep-level defects introduced by 1 MeV electron radiation in AlInGaP for multijunction space solar cells, J. Appl. Phys. 98 (2005) 1–5, https://doi.org/10.1063/1.2115095.

[27] J. Li, S.Y. Kim, D. Nam, X. Liu, J.H. Kim, H. Cheong, W. Liu, H. Li, Y. Sun, Y. Zhang, Tailoring the defects and carrier density for beyond 10% efficient CZTSe thin film solar cells, Sol. Energy Mater. Sol. Cells 159 (2017) 447–455, https://doi.org/10.1016/J.SOLMAT.2016.09.034.

[28] J. Li, X. Yu, S. Yuan, L. Yang, Z. Liu, D. Yang, Effects of oxygen related thermal donors on the performance of silicon heterojunction solar cells, Sol. Energy Mater. Sol. Cells 179 (2018) 17–21, https://doi.org/10.1016/J.SOLMAT.2018.02.006.

[29] M.A. Lourenço, Y.K. Yew, K.P. Homewood, K. Durose, H. Richter, D. Bonnet, Deep level transient spectroscopy of CdS/CdTe thin film solar cells, J. Appl. Phys. 82 (1997) 1423–1426, https://doi.org/10.1063/1.366285.

[30] I. Rimmaudo, A. Salavei, E. Artegiani, D. Menossi, M. Giarola, G. Mariotto, A. Gasparotto, A. Romeo, Improved stability of CdTe solar cells by absorber surface etching, Sol. Energy Mater. Sol. Cells 162 (2017) 127–133, https://doi.org/10.1016/J.SOLMAT.2016.12.044.

[31] A.S. Shikoh, S. Paek, A.Y. Polyakov, N.B. Smirnov, I.V. Shchemerov, D.S. Saranin, S.I. Didenko, Z. Ahmad, F. Touati, M.K. Nazeeruddin, Assessing mobile ions contributions to admittance spectra and current-voltage characteristics of 3D and 2D/3D perovskite solar cells, Sol. Energy Mater. Sol. Cells 215 (2020) 110670, https://doi.org/10.1016/J.SOLMAT.2020.110670.

[32] C.M. Ruiz, I. Rey-Stolle, I. Garcia, E. Barrigón, P. Espinet, V. Bermúdez, C. Algora, Capacitance measurements for subcell characterization in multijunction solar cells, Conf. Rec. IEEE Photovolt. Spec. Conf. (2010) 708–711, https://doi.org/10.1109/PVSC.2010.5617045.

[33] M. Rutzinger, M. Salzberger, A. Gerhard, H. Nesswetter, P. Lugli, C. G. Zimmermann, Measurement of subcell depletion layer capacitances in multijunction solar cells, Appl. Phys. Lett. 111 (2017) 183507, https://doi.org/10.1063/1.4998148.

[34] X. Zhang, J. Hu, Y. Wu, F. Lu, Direct observation of defects in triple-junction solar cell by optical deep-level transient spectroscopy, J. Phys. D Appl. Phys. 42 (2009) 145401, https://doi.org/10.1088/0022-3727/42/14/145401.

[35] C. Leon, S. Le Gall, M.-E. Gueunier-Farret, A. Brézard-Oudot, A. Jaffre, N. Moron, L. Vauche, K. Medjoubi, E.V. Vidal, C. Longeaud, J.-P. Kleider, Understanding and monitoring the capacitance-voltage technique for the characterization of tandem solar cells, Prog. Photovoltaics Res. Appl. 28 (2020) 601–608, https://doi.org/10.1002/PIP.3235.

[36] S.M. Sze, Physics of Semiconductor Devices, second ed., ume 23, Wiley-Interscience, Murray Hill, New Jersey, 1981.

[37] W.G. Oldham, S.S. Naik, Admittance of p-n junctions containing traps, Solid State Electron. 15 (1972) 1085–1096, https://doi.org/10.1016/0038-1101(72)90167-0.

[38] C. Ghezzi, Space-charge analysis for the admittance of semiconductor junctions with deep impurity levels, Appl. Phys. A 26 (1981) 191–202, https://doi.org/10.1007/BF00614756.

[39] J.L. Pautrat, B. Katircioglu, N. Magnea, D. Bensahel, J.C. Pfister, L. Revoil, Admittance spectroscopy: a powerful characterization technique for semiconductor crystals—application to ZnTe, Solid State Electron. 23 (1980) 1159–1169, https://doi.org/10.1016/0038-1101(80)90028-3.

[40] W. Shockley, J.W.T. Read, Statistics of the recombinations of holes and electrons, Phys. Rev. 87 (1952) 835, https://doi.org/10.1103/PhysRev.87.835.

[41] A.R. Peaker, V.P. Markevich, J. Coutinho, Tutorial: junction spectroscopy techniques and deep-level defects in semiconductors, J. Appl. Phys. 123 (2018) 161559, https://doi.org/10.1063/1.5011327.

[42] J.-P. Kleider, J. Alvarez, A. Brézard-Oudot, M.-E. Gueunier-Farret, O. Maslova, Revisiting the theory and usage of junction capacitance: application to high efficiency amorphous/crystalline silicon heterojunction solar cells, Sol. Energy Mater. Sol. Cells 135 (2015) 8–16, https://doi.org/10.1016/j.solmat.2014.09.002.

[43] Silvaco Atlas, User's Man. (2016).

[44] C. Leon, Adaptation des techniques de caractérisation basées sur des mesures de capacité et d'admittance aux cellules solaires multijonctions : expériences et modélisations, Energie électrique. Univ. Paris-Saclay. (2020) (Français).